



## ISTITUTO NAZIONALE DI RICERCA METROLOGICA Repository Istituzionale

Coupling of wavefront errors and jitter in the LISA interferometer: far-field propagation

*Original*

Coupling of wavefront errors and jitter in the LISA interferometer: far-field propagation / Sasso, C; Mana, G; Mottini, S. - In: CLASSICAL AND QUANTUM GRAVITY. - ISSN 0264-9381. - 35:18(2018), p. 185013. [10.1088/1361-6382/aad7f5]

*Availability:*

This version is available at: 11696/59825 since: 2019-02-14T10:41:14Z

*Publisher:*

IOP

*Published*

DOI:10.1088/1361-6382/aad7f5

*Terms of use:*

This article is made available under terms and conditions as specified in the corresponding bibliographic description in the repository

*Publisher copyright*

(Article begins on next page)

PAPER • OPEN ACCESS

## Coupling of wavefront errors and jitter in the LISA interferometer: far-field propagation

To cite this article: C P Sasso *et al* 2018 *Class. Quantum Grav.* **35** 185013

View the [article online](#) for updates and enhancements.

### Related content

- [Wavefront distortion and beam pointing for LISA](#)  
Peter L Bender
- [Wavefront errors in a two-beam interferometer](#)  
G Mana, E Massa and C P Sasso
- [Adaptive optics in the formation of optical beams and images](#)  
V P Lukin

### Recent citations

- [Coupling of wavefront errors and pointing jitter in the LISA interferometer: misalignment of the interfering wavefronts](#)  
C P Sasso *et al*



**IOP Astronomy ebooks**

Part of your publishing universe and your first choice for astronomy, astrophysics, solar physics and planetary science ebooks.

[iopscience.org/books/aas](http://iopscience.org/books/aas)

# Coupling of wavefront errors and jitter in the LISA interferometer: far-field propagation

C P Sasso<sup>1</sup>, G Mana<sup>1</sup> and S Mottini<sup>2</sup>

<sup>1</sup> INRIM—Istituto Nazionale di Ricerca Metrologica, Str. delle cacce 91, 10135 Torino, Italy

<sup>2</sup> Thales Alenia Space, Str. Antica di Collegno, 253, 10146 Torino, Italy

E-mail: [c.sasso@inrim.it](mailto:c.sasso@inrim.it)

Received 7 June 2018, revised 25 July 2018

Accepted for publication 3 August 2018

Published 29 August 2018



CrossMark

## Abstract

The Laser Interferometer Space Antenna (LISA) is a gravitational wave detector, which aims to detect  $10^{-20}$  strains in the frequency range from 0.1 mHz to 0.1 Hz. It is a constellation of three spacecrafts, an equilateral triangle with side length of  $2.5 \times 10^9$  m, where interferometry monitors the spacecraft distances. Aberrations and jitter of the wavefront sent by a spacecraft to the next combine to cause a measurement noise. The paper investigates analytically this coupling, including beam clipping and far-field propagation, and develops criteria for the assessment of the wavefront quality. It also gives the results of Monte Carlo simulations of the measurement noise for arbitrary wavefront aberrations and jitters.

Keywords: gravitational waves measurement, long baseline optical interferometry, optical far field propagation, Laser Interferometer Space Antenna (LISA)

 Supplementary material for this article is available [online](#)

(Some figures may appear in colour only in the online journal)



Original content from this work may be used under the terms of the [Creative Commons Attribution 3.0 licence](#). Any further distribution of this work must maintain attribution to the author(s) and the title of the work, journal citation and DOI.

## 1. Introduction

The spacecraft of the Laser Interferometer Space Antenna (LISA) are at the vertices of an equilateral triangle, which is in a plane inclined  $60^\circ$  with respect to the ecliptic and trails the Earth by  $20^\circ$  [1–3]. Each spacecraft is equipped with two telescopes, with associated lasers and optical systems, that transmit and receive 1064 nm beams linking the constellation’s spacecraft by interferometry. The telescope design includes four mirrors with off-axis primary and secondary mirrors to avoid back-reflection from the secondary mirror. Preliminary parameters are: primary mirror diameter 200 mm, input beam diameter 2.2 mm, magnification  $90\times$ , field of view  $\pm 8 \mu\text{rad}$  [4, 5].

A critical aspect is the picometre sensitivity required in the measurement of the spacecraft’s separation, which is  $2.5 \times 10^9$  m. In fact, the measurement aims at noise power density approaching  $1 \text{ pm}^2 \text{ Hz}^{-1}$  in the frequency interval from 0.1 mHz to 1 Hz [6]. In turns, this requires that the noise power density of the interference-signal phase approaches  $1 \mu\text{rad}^2 \text{ Hz}^{-1}$  and imposes tight requirements on the phase stability of the received wavefront [7–9].

The wavefront errors of the transmitted beam combine with the pointing jitter to originate a phase noise. In fact, because of the wavefront errors, the received wavefront deviates from a spherical one centred on the test mass and any pointing variation leads to local changes of the phase and, consequently, to apparent variations of the spacecraft distance [10, 11].

In this regard, the LISA’s telescopes are critical sub-systems, and there is a need for criteria for the quality of the transmitted wavefront, where the far-field propagation is taken into account. This underpins the specifications for the manufacturing of the telescopes and the error budget of the optical system.

Previous works carried out numerical and ray-tracing analyses to determine the errors of the received wavefront [12–14] and examined defocus [10, 15], astigmatism [16], and truncation [15] effects. We build on these investigations and give an analytical expression of the wavefront error at the receiving spacecraft—for the transmission of truncated beams having both plane and Gaussian intensity profiles—as a function of the normalised beam radius and Zernike modal amplitudes of the aberrations of the transmitted wavefront. Eventually, we investigated the phase noise of the received wavefront and took advantage of the results obtained to carry out Monte Carlo calculations for arbitrary aberrations of the transmitted wavefront and variances of the horizontal and vertical tilts, which are related to the beam-pointing jitter. The piston aberration, which is related to the dimensional stability of the telescope, was investigated in [17] and will not be considered here.

## 2. Far-field propagation of the wavefront error

By using the scalar and paraxial approximations, we describe the monochromatic optical field propagating between the spacecraft,

$$E(\mathbf{r}, z; t) = u(\mathbf{r}; z)e^{-i(kz - \omega t)}, \quad (1)$$

by means of its complex amplitude  $u(\mathbf{r}; z)$ , where  $z$  is the propagation distance,  $\mathbf{r} = \{x, y\}$  are the transverse coordinates,  $\omega$  is the angular frequency,  $k = \omega/c = 2\pi/\lambda$  is the wave number,  $\lambda = 1064$  nm is the wavelength, and the width of the  $u(\mathbf{r}; z)$  spectrum is much less than  $k$ . The light takes about 8 s to travel between the spacecraft. Therefore, because of the orbital dynamics of the constellation, the transmitted beam needs to point ahead to the position where the other spacecraft is observed, which corresponds to an angle varying up to about  $\pm 6 \mu\text{rad}$ . Therefore, in (1), the  $z$  axis joins the centre of the transmitting telescope to that of the

receiving one at about 8 s in the future. Eventually, we describe the complex amplitude of the beam leaving the transmitting spacecraft by

$$u(\mathbf{r}; 0) = u_0(\mathbf{r})e^{i\mathfrak{w}_0(\mathbf{r})}, \quad (2)$$

where  $\mathfrak{w}_0(\mathbf{r})$  is a small and zero-mean wavefront error.

### 2.1. Reciprocal space propagation

By using the reciprocal-space representation, the paraxial propagation in free space of the complex amplitude (2) truncated by the telescope aperture  $\mathcal{A}$  (a disk having typically 0.1 m radius) is given by [18]

$$\tilde{u}(\boldsymbol{\kappa}; z) = U(\boldsymbol{\kappa}; z)\tilde{u}_0(\boldsymbol{\kappa}), \quad (3)$$

where  $\boldsymbol{\kappa}$  is the wave-vector conjugate to  $\mathbf{r}$ ,

$$\tilde{u}_0(\boldsymbol{\kappa}) = \frac{1}{2\pi} \int_{\mathcal{A}} e^{i\boldsymbol{\kappa}\boldsymbol{\xi}} u_0(\boldsymbol{\xi}) e^{i\mathfrak{w}_0(\boldsymbol{\xi})} d\boldsymbol{\xi}, \quad (4)$$

is the  $u(\boldsymbol{\xi}; 0)$  spectrum,  $\boldsymbol{\xi}$  is a position vector in the input plane, and

$$U(\boldsymbol{\kappa}; z) = \exp\left(\frac{i\boldsymbol{\kappa}^2 z}{2k}\right) \quad (5)$$

is the reciprocal-space representation of the paraxial approximation of the free-space propagator. In the limit when  $kz \rightarrow \infty$ , by calculating the inverse Fourier transform of (3) by the steepest-descent method, we obtain

$$u(\mathbf{r}; z) \approx \frac{ike^{-ikr^2/(2z)}}{2\pi z} \tilde{u}_0(k\mathbf{r}/z), \quad (6)$$

where  $\exp[-ikr^2/(2z)]/z$  is a spherical wave and  $\tilde{u}_0(k\mathbf{r}/z)$  takes diffraction into account. As expected, in the far field the intensity of the optical signal is the square modulus of the Fourier transform, scaled by the distance  $z$ .

### 2.2. Direct space propagation

The paraxial propagation in free space is given by the Rayleigh–Sommerfeld integral [18]

$$u(\mathbf{r}; z) = \int_{\mathcal{A}} U(\mathbf{r}; \boldsymbol{\xi}) u_0(\boldsymbol{\xi}) e^{i\mathfrak{w}_0(\boldsymbol{\xi})} d\boldsymbol{\xi}, \quad (7)$$

where

$$U(\mathbf{r}; \boldsymbol{\xi}) = \frac{ike^{-ik|\mathbf{r}-\boldsymbol{\xi}|^2/(2z)}}{2\pi z}, \quad (8)$$

is the direct-space representation of (5), the integration is carried out on the  $z = 0$  input-plane, and  $\boldsymbol{\xi}$  and  $\mathbf{r}$  are position vectors in the input and output planes, respectively. Since (5) and (8) are only different representations (in the reciprocal and direct spaces) of the same kernel,  $\tilde{u}(\boldsymbol{\kappa}; z)$  and  $u(\mathbf{r}; z)$ —see (3) and (7)—are solutions of the same paraxial equation and forms a Fourier transform pair.

Since  $k\xi^2/(2z) \ll \mathfrak{w}_0(\boldsymbol{\xi})$ , once (8) is substituted in (7) the far-field amplitude of the transmitted beam is

$$u(\mathbf{r}; z) \approx \frac{ik e^{-ikr^2/(2z)}}{2\pi z} \int_{\mathcal{A}} e^{ik\mathbf{r}\cdot\boldsymbol{\xi}/z} u_0(\boldsymbol{\xi}) e^{i w_0(\boldsymbol{\xi})} d\boldsymbol{\xi} \quad (9)$$

which, obviously, is identical to (6). It is worth noting that, for any given spacecraft's separation  $z$ , the neglected  $k\xi^2/(2z)$  kernel-phase corresponds to an additional defocus of  $w_0(\boldsymbol{\xi})$ , and can be included among the perturbations of the waveform that will be discussed below in the document.

### 2.3. On-axis propagation

On the axis of the receiving telescope, the far-field amplitude is

$$u(0; z) = \frac{ik}{2\pi z} \int_{\mathcal{A}} u_0(\boldsymbol{\xi}) e^{i w_0(\boldsymbol{\xi})} d\boldsymbol{\xi}. \quad (10)$$

We observe that, by limiting the far-field calculation to the input aperture of the receiving telescope (having typically 0.1 m radius), the extremal values of the  $k\mathbf{r}\cdot\boldsymbol{\xi}/z$  phase of the (9)'s kernel are  $\pm 30 \mu\text{rad}$ , to be compared with the  $w_0(\boldsymbol{\xi})$  phase which, in the case of  $\lambda/20$  wavefront errors, is bounded by  $\pm 150 \mu\text{rad}$ . By neglecting these extrema, the on-axis amplitude is representative of the whole received field and, to within this approximation, the received wavefront is a spherical one having a phase given by the argument of (10).

For any given spacecraft's separation  $z$ , the neglected  $k\mathbf{r}\cdot\boldsymbol{\xi}/z$  phase corresponds to a tilt by the angle  $\mathbf{r}/z$  of  $w_0(\boldsymbol{\xi})$ . Therefore, the off-axis value  $u(\mathbf{r}; z)$  is identical to the on-axis amplitude calculated with the transmitted wavefront tilted by  $\mathbf{r}/z$ .

### 2.4. Series expansion of the complex amplitude

By assuming  $w_0(\boldsymbol{\xi}) \ll 1$  the exponential term of equation (2) approximates to

$$e^{i w_0(\boldsymbol{\xi})} \approx 1 + i w_0(\boldsymbol{\xi}) - \frac{1}{2} w_0^2(\boldsymbol{\xi}) - \frac{i}{6} w_0^3(\boldsymbol{\xi}) + \dots, \quad (11)$$

and apart the non-essential  $ik/(2\pi z)$  factor, the on-axis far field is

$$\begin{aligned} u(0; z) \approx & \int_{\mathcal{A}} u_0(\boldsymbol{\xi}) d\boldsymbol{\xi} + i \int_{\mathcal{A}} w_0(\boldsymbol{\xi}) u_0(\boldsymbol{\xi}) d\boldsymbol{\xi} \\ & - \frac{1}{2} \int_{\mathcal{A}} w_0^2(\boldsymbol{\xi}) u_0(\boldsymbol{\xi}) d\boldsymbol{\xi} - \frac{i}{6} \int_{\mathcal{A}} w_0^3(\boldsymbol{\xi}) u_0(\boldsymbol{\xi}) d\boldsymbol{\xi} + \dots \end{aligned} \quad (12)$$

### 2.5. Zernike modal amplitudes

Since the transmitted beam is truncated by a circular aperture, having typically 0.1 m radius, a useful way to express the wavefront errors is by the modal amplitudes of the Zernike polynomials, which are a complete set of orthogonal basis functions over the unit disk. Therefore, let us consider a circular aperture  $\mathcal{A}$  having radius  $r_0$  and write the wavefront errors in terms of the Zernike polynomials,

$$w_0(\mathbf{r}) = \sum_{n=1}^{\infty} \sum_{m=-n}^n z_n^m R_n^{|m|}(\rho) e^{im\theta}, \quad (13)$$

where  $R_n^{|m|}(\rho) = 0$  for all  $n - |m|$  odd or negative,  $\rho = r/r_0$ ,  $\theta$  is the azimuth, and  $z_n^m$  is a complex number that must fulfill the relation  $z_n^{-m} = z_n^{m*}$  in order (13) to be real. Hence,  $z_n^0$  is real and, if  $m \neq 0$ ,

$$z_n^{\pm m} = |z_n^m| e^{\pm i\theta_n^m}, \quad (14)$$

where  $\theta_n^m$  is the azimuth rotation of the reference system of the polynomials with respect to that of the telescope. The radial functions are given by

$$R_n^{|m|}(\rho) = (-1)^{(n-|m|)/2} \rho^{|m|} P_{(n-|m|)/2}^{(|m|,0)}(1-2\rho^2), \quad (15)$$

where  $P_k^{(\alpha,\beta)}$  is the Jacobi polynomial of degree  $k$ , and satisfy the orthogonality relation

$$\int_0^1 R_n^{|m|}(\rho) R_{n'}^{|m|}(\rho) \rho \, d\rho = \frac{\delta_{n,n'} R_n^{|m|}(1)}{2(n+1)}. \quad (16)$$

## 2.6. Tilt aberration

According to (1) and (2), a wavefront tilt by a small angle  $\boldsymbol{\alpha} = \alpha[\cos(\beta), \sin(\beta)]^T$  about an axis lying in a plane orthogonal to  $z$  and having azimuth  $\beta$  is implemented by the transformation

$$w_0(r, \theta) \rightarrow w_0(r, \theta) + k\boldsymbol{\xi} \cdot \boldsymbol{\alpha} = w_0(r, \theta) + kr\alpha \cos(\theta - \beta), \quad (17)$$

where  $\boldsymbol{\xi} = r[\cos(\theta), \sin(\theta)]^T$  and we considered only the first order term. Therefore, the  $n = 1$  term of the Zernike expansion (13),

$$z_1^{-1} \rho e^{-i\theta} + z_1^1 \rho e^{i\theta} = 2|z_1^1| \rho \cos(\theta + \theta_1^1), \quad (18)$$

where  $\theta_1^1 = -\beta$ , takes the wavefront tilt into account and

$$\alpha = \frac{2|z_1^1|}{kr_0}. \quad (19)$$

It is worth noting that  $\boldsymbol{\alpha}$ , which identifies the pointing of  $u_0(\boldsymbol{\xi})$ , approximates the deviation of the beam-propagation direction from the  $z$  axis and, since  $\lambda = 1064$  nm and  $r_0 \approx 0.1$  m, the approximation (11) is valid if  $\alpha \lesssim 1$   $\mu$ rad.

## 3. Flat intensity profile

### 3.1. Received wavefront

Let  $u_0(\boldsymbol{\xi}) = 1$ , where we used a unit and dimensionless power density of the transmitted beam. To calculate the errors of the received wavefront, we introduce the notations

$$a_0 = \frac{1}{\pi r_0^2} \int_{\mathcal{A}} u_0(\boldsymbol{\xi}) \, d\boldsymbol{\xi} = 1, \quad (20a)$$

$$a_1 = \frac{1}{\pi r_0^2} \int_{\mathcal{A}} w_0(\boldsymbol{\xi}) u_0(\boldsymbol{\xi}) \, d\boldsymbol{\xi} = 0, \quad (20b)$$

$$a_2 = -\frac{1}{2\pi r_0^2} \int_{\mathcal{A}} w_0^2(\boldsymbol{\xi}) u_0(\boldsymbol{\xi}) \, d\boldsymbol{\xi}, \quad (20c)$$

**Table 1.** Coefficients of the (24a)–(24c) polynomials.

B	C	D	E	F	G	H
−1/2	−1/6	−1/3	−1/6	−1/3	−1/5	0

and

$$a_3 = -\frac{1}{6\pi r_0^2} \int_{\mathcal{A}} w_0^3(\xi) u_0(\xi) d\xi. \quad (20d)$$

By rewriting (12) as

$$u(0; z) \approx \pi r^2 (a_0 + ia_1 + a_2 + ia_3), \quad (21)$$

up to third order of the Zernike modal amplitudes of the transmitted-wavefront aberrations, the wavefront errors at the receiving spacecraft,  $w(0; z) = \arg[u(0; z)]$ , is approximated by

$$w(0; z) \approx \frac{\text{Im}[u(0; z)]}{\text{Re}[u(0; z)]} = \frac{a_1 + a_3}{a_0 + a_2} \approx a_3(1 - a_2), \quad (22)$$

which expresses the excess (defect) of the optical distance between the spacecraft with respect to their geometric distance. Within the perturbative approach adopted, equation (22) shows that the errors of the received wavefront depend on the modal amplitudes of the Zernike spectrum of the transmitted-wavefront only whether at least the third perturbative-order is taken into account.

By limiting the wavefront aberration to tilt, defocus, astigmatism, coma, trefoil, and spherical—that is by considering in (13) only the modal amplitudes  $z_1^1, z_2^0, z_2^2, z_3^1, z_3^3$ , and  $z_4^0$ —we obtain

$$w(0, z) = b_0 + b_1 |z_1^1| + b_2 |z_1^1|^2, \quad (23)$$

where we used (22) and made explicit the dependence on the amplitude of the tilt,  $|z_1^1| = kr_0\alpha/2$ , to describe the coupling of the  $\alpha$ 's jitter to the errors of the transmitted wavefront. To obtain the  $b_i$  coefficients, we have carried out the integrations (20a)–(20d) with the aid of Mathematica [19]. The code is available in the supplementary material ([stacks.iop.org/CQG/35/185013/mmedia](https://stacks.iop.org/CQG/35/185013/mmedia)). By retaining only the lowest order terms, they are

$$\begin{aligned} b_0 = & -\frac{1}{60} z_2^0 (10|z_2^2|^2 + |z_3^1|^2 + 9|z_3^3|^2) - \frac{2}{15} |z_2^2| |z_3^1|^2 \cos(\theta_2^2 - 2\theta_3^1) \\ & - \frac{1}{5} |z_2^2| |z_3^1| |z_3^3| \cos(\theta_3^3 - \theta_2^2 - \theta_3^1) \\ & - \left( \frac{1}{15} |z_2^0|^2 + \frac{1}{30} |z_2^2|^2 + \frac{1}{20} |z_3^1|^2 + \frac{1}{20} |z_3^3|^2 + \frac{1}{105} |z_4^0|^2 \right) z_4^0, \end{aligned} \quad (24a)$$

$$\begin{aligned} b_1 = & B |z_2^2| |z_3^3| \cos(\theta_3^3 - \theta_2^2 - \theta_1^1) + C |z_2^2| |z_3^1| \cos(\theta_2^2 - \theta_3^1 - \theta_1^1) \\ & + D |z_3^1| z_2^0 \cos(\theta_3^1 - \theta_1^1) + G |z_3^1| z_4^0 \cos(\theta_3^1 - \theta_1^1), \end{aligned} \quad (24b)$$

$$b_2 = E z_2^0 + F |z_2^2| \cos(\theta_2^2 - 2\theta_1^1) + H z_4^0. \quad (24c)$$

The  $B, C \dots H$  values are given in table 1.

### 3.2. Received power density

By remembering (10) and (12) and after normalizing to the aberration-free density  $[\pi k r_0^2 / (2\pi z)]^2$ , the received power density is

$$I(0; z) \approx 1 - \frac{k^2 r_0^2}{4} \alpha^2 - \sum_{n=2}^{\infty} \sum_{m=-n}^n \frac{|z_n^m|^2 R_n^{|m|}(1)}{n+1}, \quad (25)$$

where we used  $|z_1^1| = k r_0 \alpha / 2$ . The received power density is maximum when  $\alpha = 0$ , that is, the beam is pointed along the  $z$  axis, and decreases quadratically with the pointing error.

## 4. Gaussian intensity profile

### 4.1. Received wavefront

Let  $u_0(\xi) = \exp(-r^2/w^2)$ , where the power density is unitary. By following the same steps as in section 3.1, we redefine the symbols in (20a)–(20d) as

$$a_0 = 1 - e^{-r_0^2/w^2} = \frac{1}{\pi w^2} \int_{\mathcal{A}} u_0(\xi) d\xi, \quad (26a)$$

$$a_1 = \frac{1}{\pi w^2} \int_{\mathcal{A}} w_0(\xi) u_0(\xi) d\xi, \quad (26b)$$

$$a_2 = -\frac{1}{2\pi w^2} \int_{\mathcal{A}} w_0^2(\xi) u_0(\xi) d\xi, \quad (26c)$$

and

$$a_3 = -\frac{1}{6\pi w^2} \int_{\mathcal{A}} w_0^3(\xi) u_0(\xi) d\xi, \quad (26d)$$

and rewrite (12) as

$$u(0; z) \approx \pi w^2 (a_0 + i a_1 + a_2 + i a_3). \quad (27)$$

Since  $\text{Im}[u(0; z)] \ll \text{Re}[u(0; z)]$ —no matter what the  $w$  value may be—and both the limits of  $a_2 / (1 - e^{-r_0^2/w^2})$  when  $r_0/w \rightarrow \infty$  and  $r_0/w \rightarrow 0$  are finite, the wavefront error at the receiving spacecraft can be approximated up to third order of the Zernike modal amplitudes of the transmitted-wavefront aberrations as

$$\begin{aligned} w(0; z) &\approx \frac{\text{Im}[u(0; z)]}{\text{Re}[u(0; z)]} = -\frac{a_1 + a_3}{a_0 + a_2} \\ &\approx \frac{(a_1 + a_3)(1 - e^{-1/w'^2} - a_2)}{(1 - e^{-1/w'^2})^2}, \end{aligned} \quad (28)$$

where  $w' = r_0/w$ . Hence, by limiting again the wavefront aberration to tilt, defocus, astigmatism, coma, trefoil, and spherical, and by carrying out the relevant algebraic calculations,

$$w(0, z) = b_0 + b_1 |z_1^1| + b_2 |z_1^1|^2, \quad (29)$$

where we used (28). To obtain the  $b_i$  coefficients, we carried out the integrations (26b)–(26d) with the aid of Mathematica [19]. The code is available in the supplementary material. By retaining only the lowest order terms, they are

$$b_0 = A_2 z_2^0 + A_4 z_4^0, \quad (30a)$$

$$b_1 = B |z_2^2| |z_3^3| \cos(\theta_3^3 - \theta_2^2 - \theta_1^1) + C |z_2^2| |z_3^1| \cos(\theta_2^2 - \theta_3^1 - \theta_1^1) \\ + D z_2^0 |z_3^1| \cos(\theta_3^1 - \theta_1^1) + G z_4^0 |z_3^1| \cos(\theta_3^1 - \theta_1^1), \quad (30b)$$

$$b_2 = E z_2^0 + F |z_2^2| \cos(\theta_2^2 - 2\theta_1^1) + H z_4^0, \quad (30c)$$

where, by measuring the beam radius  $w$  in terms of the telescope aperture  $r_0$ ,

$$A_2 = \frac{1 + e^{1/w'^2} + 2(1 - e^{1/w'^2})w'^2}{1 - e^{1/w'^2}}, \quad (31a)$$

$$A_4 = \frac{1 - e^{1/w'^2} + 6(1 + e^{1/w'^2})w'^2 + 12(1 - e^{1/w'^2})w'^4}{1 - e^{1/w'^2}}, \quad (31b)$$

$$B = -\frac{2[1 + 3w'^2 + 6w'^4 + 6(1 - e^{1/w'^2})w'^6]}{1 - e^{1/w'^2}}, \quad (31c)$$

$$C = -\frac{2[1 + 5w'^2 + 2(7 + 2e^{1/w'^2})w'^4 + 18(1 - e^{1/w'^2})w'^6]}{1 - e^{1/w'^2}}, \quad (31d)$$

$$D = \frac{4 \left[ e^{1/w'^2} + 6e^{1/w'^2} w'^2 - 2(2 - e^{1/w'^2} - e^{2/w'^2})w'^4 - 12(1 - e^{1/w'^2})^2 w'^6 \right]}{(1 - e^{1/w'^2})^2}, \quad (31e)$$

$$G = \frac{24 \left[ e^{1/w'^2} w'^2 - (2 - 9e^{1/w'^2} + e^{2/w'^2})w'^4 - 2(7 - 2e^{1/w'^2} - 5e^{2/w'^2})w'^6 - 30(1 - e^{1/w'^2})^2 w'^8 \right]}{(1 - e^{1/w'^2})^2}, \quad (31f)$$

$$E = \frac{2[e^{1/w'^2} - (1 - e^{2/w'^2})^2 w'^4]}{(1 - e^{1/w'^2})^2}, \quad (31g)$$

$$F = -\frac{1 + 2w'^2 + 2(1 - e^{1/w'^2})w'^4}{1 - e^{1/w'^2}}, \quad (31h)$$

$$H = \frac{6[2e^{1/w'^2} w'^2 - (1 - e^{2/w'^2})w'^4 - 4(1 - e^{1/w'^2})^2 w'^6]}{(1 - e^{1/w'^2})^2}. \quad (31i)$$

Figure 1 shows the  $A_2$ ,  $A_4$ ,  $B$ , ... coefficients versus the beam radius  $w$ . Also in this case, (29) describes the coupling of the  $\alpha$ 's jitter to the errors of the transmitted wavefront.

Contrary to the truncated plane-wave case, since  $a_1 \neq 0$ , the wavefront error at the receiving spacecraft (29) displays a first order dependence on the aberrations of the transmitted wavefront—namely defocus, spherical aberration, and higher order axially symmetric aberrations. As shown in figure 1, when  $w' \rightarrow 0$ , the received wavefront is insensitive to the beam pointing. In fact, in this case, the received wavefront is spherical and centred in the origin of the input plane. Figure 1 shows also that, when  $w' \rightarrow \infty$ , (29) converges to the truncated plane-wave solution (22), as expected.

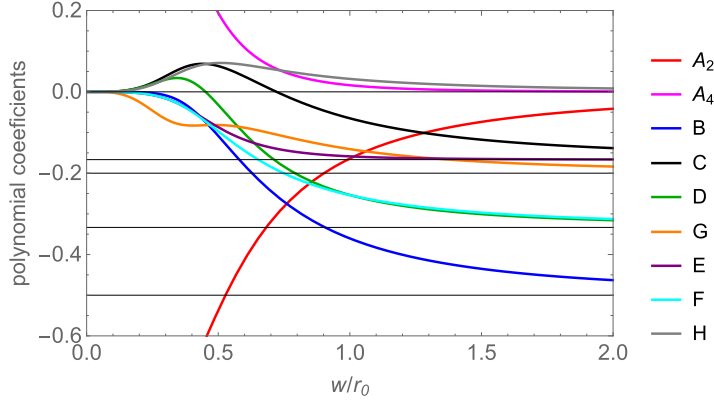


**Figure 1.** Coefficients of the (30a)–(30c) polynomials versus the  $w/r_0$  ratio. The horizontal lines are the asymptotic values given in table 1 for the transmission of a flat intensity-profile. The limits of  $A_2$  and  $A_4$  when  $w/r_0 \rightarrow 0$  are  $\pm 1$ .

#### 4.2. Received power density

By remembering (10) and (12), observing that (up to the second order of the Zernike modal amplitudes of the transmitted-wavefront aberrations)

$$\begin{aligned}
 |u(0; z)|^2 &\approx \frac{\pi^2 w^4 |a_0 + ia_1 + a_2|^2 k^2}{(2\pi z)^2} \\
 &\approx \frac{\pi^2 w^4 |a_0^2 + 2a_0 a_2 + a_1^2|^2 k^2}{(2\pi z)^2} \\
 &\approx \frac{\pi^2 w^4 [(1 - e^{-1/w^2})^2 + 2(1 - e^{-1/w^2})a_2 + a_1^2] k^2}{(2\pi z)^2}, \quad (32)
 \end{aligned}$$

and after normalizing to the aberration-free density  $[\pi k w^2 (1 - e^{-1/w^2}) / (2\pi z)]^2$ , the received power density is

$$I(0; z) \approx 1 + c_1 |z_3^1| [\cos(\theta_3^1) \zeta_x + \sin(\theta_3^1) \zeta_y] - c_2 (\zeta_x^2 + \zeta_y^2). \quad (33)$$

In (33),  $\zeta_x = |z_1^1| \cos(\theta_1^1)$  and  $\zeta_y = |z_1^1| \sin(\theta_1^1)$  are the horizontal and vertical tilts, and

$$c_1 = -\frac{4[1 + 2(2 + e^{1/w^2})w'^2 + 6(1 - e^{1/w^2})w'^4]}{1 - e^{-1/w^2}} \quad (34a)$$

$$c_2 = \frac{2[1 + (1 - e^{1/w^2})w'^2]}{1 - e^{-1/w^2}}. \quad (34b)$$

To obtain these coefficients, we carried out the symbolical calculations with the aid of Mathematica [19]; the code is available in the supplementary material.

Figure 2 shows the coefficients (34a) and (34b) versus the beam radius  $w$ . When  $w \rightarrow \infty$ , the received power density reduces to the plane-wave expression (25); when  $w \rightarrow 0$ , which corresponds to the transmission of a spherical wave, it is independent on the beam pointing, as expected.

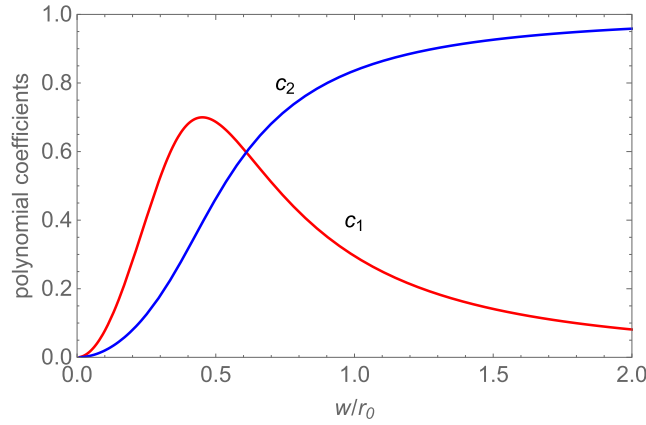


**Figure 2.** Coefficients of the polynomial (33).

The power density is maximum when

$$\zeta_x = \frac{c_1 |z_3^1| \cos(\theta_3^1)}{2c_2} \quad (35a)$$

$$\zeta_y = \frac{c_1 |z_3^1| \sin(\theta_3^1)}{2c_2}. \quad (35b)$$

In the absence of coma, whose amplitude is set by the coefficient  $z_3^1$ , the maximum is on the telescope axis. The deviation that occurs when  $z_3^1 \neq 0$  depends on the ratio between the beam and aperture radii and mirrors the beam's perception of a wavefront tilt due to the coma.

## 5. Phase noise

As shown in section 2.6, the pointing jitter of the transmitted beam with respect to the  $z$  axis translates in a jitter of the wavefront tilt-aberration. Therefore, let the horizontal and vertical tilts

$$\zeta_x = |z_1^1| \cos(\theta_1^1) = kr_0 \alpha_x / 2, \quad (36a)$$

$$\zeta_y = |z_1^1| \sin(\theta_1^1) = kr_0 \alpha_y / 2, \quad (36b)$$

where  $\alpha_x$  and  $\alpha_y$  are the horizontal and vertical pointing components, be normal uncorrelated white noises having  $\zeta_0 = (\zeta_{0x}, \zeta_{0y})$  mean (identifying the nominal pointing) and  $\sigma_x^2$  and  $\sigma_y^2$  variances. In terms of  $\zeta_x$  and  $\zeta_y$ , the wavefront error at the receiving spacecraft (29) is

$$w(0; z) = b_{00} + b_{10}\zeta_x + b_{20}\zeta_x^2 + b_{01}\zeta_y + b_{02}\zeta_y^2 + b_{11}\zeta_x\zeta_y, \quad (37)$$

where

$$b_{00} = A_2 z_2^0 + A_4 z_4^0, \quad (38a)$$

$$b_{10} = B \cos(\theta_3^3 - \theta_2^2) |z_3^3| |z_2^2| + C \cos(\theta_2^2 - \theta_3^1) |z_3^1| |z_2^2| \\ + D \cos(\theta_3^1) |z_3^1| |z_2^0| + G \cos(\theta_3^1) |z_3^1| |z_4^0|, \quad (38b)$$

$$b_{01} = B \sin(\theta_3^3 - \theta_2^2) |z_3^3| |z_2^2| + C \sin(\theta_2^2 - \theta_3^1) |z_3^1| |z_2^2| \\ + D \sin(\theta_3^1) |z_3^1| |z_2^0| + G \sin(\theta_3^1) |z_3^1| |z_4^0|, \quad (38c)$$

$$b_{20} = E z_2^0 + F \cos(\theta_2^2) |z_2^2| + H z_4^0, \quad (38d)$$

$$b_{02} = E z_2^0 - F \cos(\theta_2^2) |z_2^2| + H z_4^0, \quad (38e)$$

$$b_{11} = 2F \sin(\theta_2^2) |z_2^2|, \quad (38f)$$

and we carried out the reparametrization of  $w(0; z)$  with the aid of Mathematica [19]. The code is available in the supplementary material.

By linearization of (37), the standard deviation of the phase noise induced by the wavefront jitter is approximated by

$$\sigma_w \approx \sqrt{(b_{10} + 2b_{20}\zeta_{0x} + b_{11}\zeta_{0y})^2 \sigma_x^2 + (b_{01} + 2b_{02}\zeta_{0y} + b_{11}\zeta_{0x})^2 \sigma_y^2}. \quad (39)$$

The phase noise is minimum—actually, it nullifies—when the transmitted wavefront jitters about the stationary point of (37), that is, when the nominal pointing is given by

$$\zeta_{0x} = \frac{b_{01}b_{11} - 2b_{10}b_{02}}{4b_{02}b_{20} - b_{11}^2}, \quad (40a)$$

$$\zeta_{0y} = \frac{b_{10}b_{11} - 2b_{01}b_{20}}{4b_{02}b_{20} - b_{11}^2}. \quad (40b)$$

Provided that it is not incompatible with the power-transmission requirement, (40a) and (40b) identify the optimal pointing. It must be observed that the exact expression of  $\sigma_w^2$ , obtained by the computation of the relevant integral, removes its nullifying.

As pointed out at the end of section 2.3, the off-axis errors of the received wavefront,  $w(\mathbf{r}; z)$ , are identical to the on-axis error (37) as long as the transmitted wavefront is tilted by  $\boldsymbol{\alpha} = \mathbf{r}/z$ . Therefore, when the beam is pointed according to (40a) and (40b), the deviation of the mean curvature of the received wavefront from that of a sphere centered in the origin of the transmitting aperture, that is responsible for the coupling of the phase error to jitter, is half the trace of the Hessian matrix of (37). Hence,

$$\Delta\mathcal{K} = (b_{02} + b_{20}) \left( \frac{kr_0}{2z} \right)^2 = \left( \frac{kr_0}{z} \right)^2 \frac{Ez_2^0 + Hz_4^0}{2}, \quad (41)$$

where, to differentiate with respect to  $x$  and  $y$ , we used (36a) and (36b) and  $\mathbf{r} = \boldsymbol{\alpha}z$ . Therefore, the defocus of the transmitted wavefront could be adjusted to reduce the phase noise.

It must be noted that, if the attitude jitter of the transmitting spacecraft is  $\boldsymbol{\beta} = (\beta_x, \beta_y)$ , the phase noise  $-kz_0\beta^2/2$ , where  $z_0$  is the distance of the input-plane origin from the test mass and the negative sign is consistent with the negative retardation in (1), must be added to (37). This term takes the variation of the spacecraft's separation (measured along the  $z$  axis) into account. Eventually, since  $\boldsymbol{\beta}$  has zero mean, it does not affect the linearized version of (37) nor the approximate variance-calculation (39).

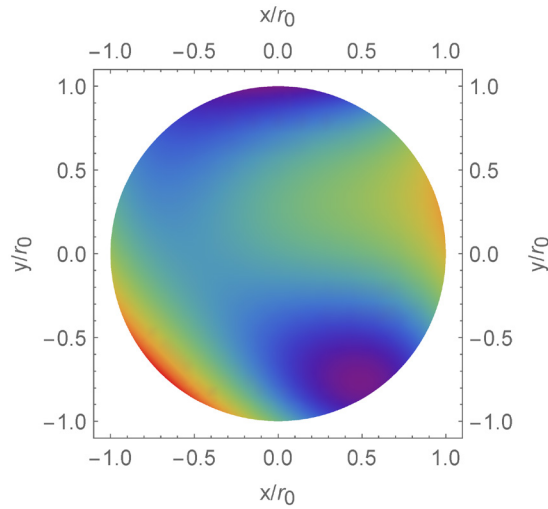


**Figure 3.** Transmitted wavefront. The rainbow extends from  $-26.6$  nm (violet) to  $+26.6$  nm (red). The Zernike modal amplitudes are given in table 2.

**Table 2.** Zernike modal amplitudes of the wavefront error shown in figure 3 (left).

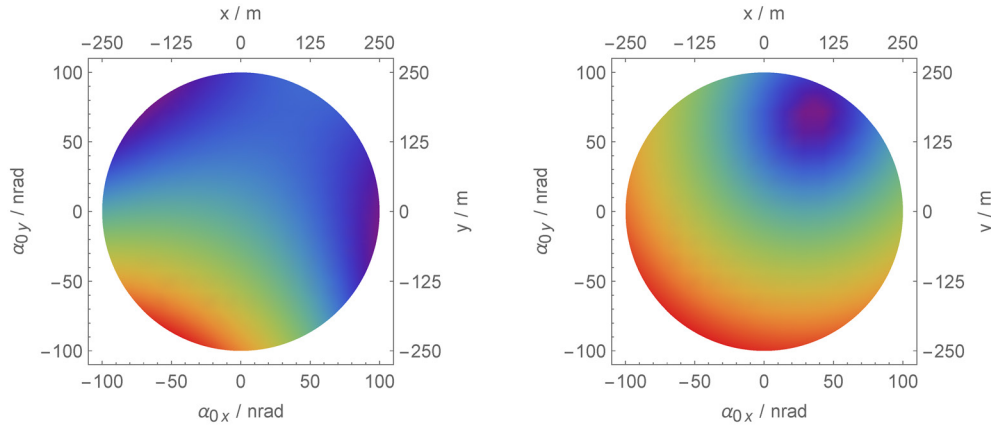
$z_2^0$	$ z_2^2 $	$ z_3^1 $	$ z_3^3 $	$z_4^0$	Unit
1.71	12.6	6.54	5.46	3.53	nm
—	$\theta_2^2$	$\theta_3^1$	$\theta_3^3$	—	Unit
—	-0.97	1.95	-0.26	—	rad

## 6. Numerical simulation

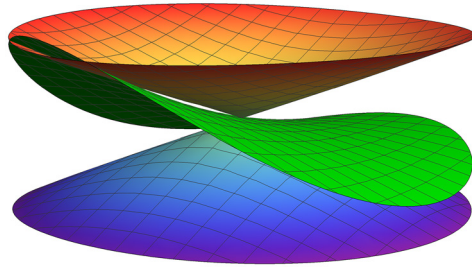
We estimated the phase noise of the received wavefront by using a Monte Carlo simulation to model the coupling between the wavefront jitter and errors. In the simulation, we randomly draw the real and imaginary parts (the latter representing the azimuthal rotation of the polynomial system of reference) of the Zernike modal amplitudes— $z_2^0$ ,  $z_2^2$ ,  $z_3^1$ ,  $z_3^3$ , and  $z_4^0$ —of the transmitted wavefront from zero-mean Gaussian distributions having the same variance and constrained to a  $\lambda/20$  peak-to-valley wavefront deviation from a plane. We set the beam wavelength and the radius of the telescope aperture to  $\lambda = 1064$  nm and  $r_0 = 0.1$  m, respectively. The normalised radius  $w/r_0$  of the transmitted beam was set to one.

Figure 3 gives an example of the randomly generated wavefronts; its Zernike modal amplitudes are given in table 2. The wavefront errors (37) and phase noise (39) at the receiving spacecraft are shown in figure 4 as a function of the horizontal and vertical tilts of the transmitted wavefront,  $\alpha_{0x}$  and  $\alpha_{0y}$  (i.e. the pointing deviations from the  $z$  axis), and of  $x = \alpha_{0x}z$  and  $y = \alpha_{0y}z$  (i.e. the transverse coordinates at the receiving telescope, see the end of section 2.3).

On the average, the errors of the received wavefront are null and bounded as shown in figure 5. By observing that, as discussed in section 2.3, a 250 m radius at the receiving telescope is equivalent to a 100 nrad tilt of the transmitted wavefront, the  $\pm 7/250$  pm  $m^{-1}$  bounds



**Figure 4.** Errors (left) and phase noise (right) of the received wavefront.  $\alpha_{0x}$  and  $\alpha_{0y}$  are the mean horizontal and vertical tilts of the transmitted wavefront, where the origin identifies the  $z$  axis.  $x = \alpha_{0x}z$  and  $y = \alpha_{0y}z$  are the transverse coordinates at the receiving telescope. The rainbows range from  $-7$  pm to  $+7$  pm (left) and from  $0.0$  pm to  $1.1$  pm (right). The (horizontal and vertical) tilt jitters of the transmitted wavefront (10 nrad standard deviation) are white and uncorrelated. The transmitted wavefront is given in figure 3, and the Zernike modal amplitudes are given in table 2.



**Figure 5.** Upper and lower bounds (standard deviations) of the received-wavefront errors. The plot region is a disk having 250 m radius. The colours range from  $-7$  pm to  $+7$  pm. The errors of the transmitted wavefront are constrained to  $\lambda/20$ . The bounds are calculated over  $10^4$  Monte Carlo simulations. An exemplary wavefront error (figure 4 left) is also shown (green).

corresponds to a  $w(0; z)$  sensitivity to the tilt equal to  $0.07$  pm nrad $^{-1}$ . Figure 6 shows the parabolic approximation (33) of the received power.

The histograms of the pointing directions maximising the transmitted power and those minimising the phase noise of the received wavefront are shown in figure 7 (left and right). Figure 8 shows the distribution of the transmitted power (33) when the pointing direction is chosen in such a way to minimise the phase noise of the received wavefront. In the majority of the Monte Carlo simulations—actually, 95%—the power loss is less than 10%, but there are cases—actually, 2.5%—where the power loss is higher than 50%. Also, to calculate the transmitted power, we used the parabolic approximation (33). Therefore, though the left tail of the histogram is a clue of troubles, the actual loss value reported must be handled with care.

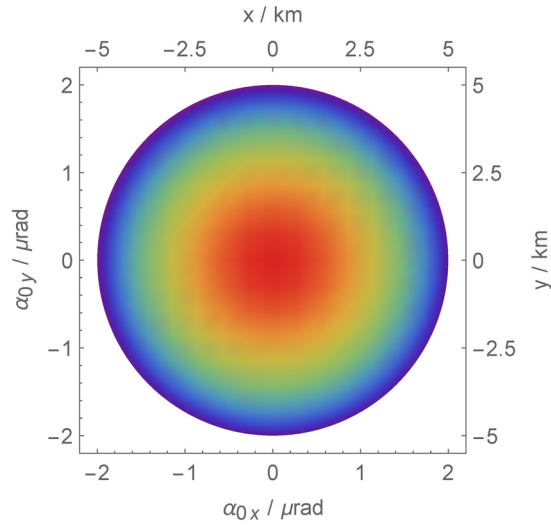


**Figure 6.** Received fractional power.  $\alpha_{0x}$  and  $\alpha_{0y}$  are the horizontal and vertical tilts of the transmitted wavefront, where the origin identifies the  $z$  axis.  $x = \alpha_{0x}z$  and  $y = \alpha_{0y}z$  are the transverse coordinates at the receiving telescope. The transmitted wavefront is given in figure 3; the Zernike modal amplitudes are given in table 2. The colours range from 0.7 (violet) to 1 (red).

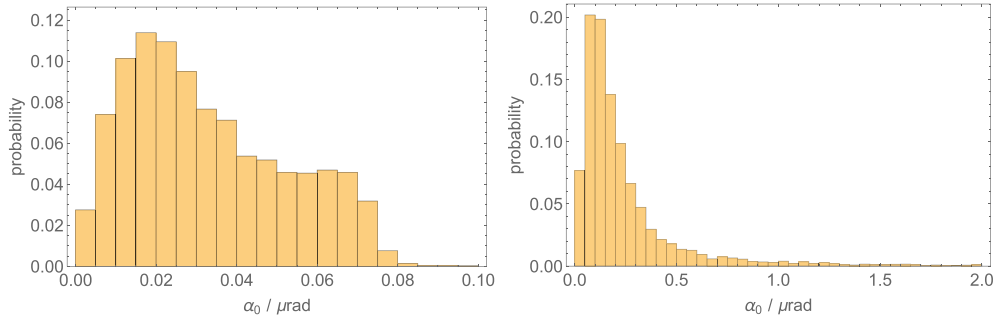


**Figure 7.** Histograms of  $10^4$  Monte Carlo calculations of the pointing directions  $\alpha_0$  maximising the transmitted power (left) and minimising the phase noise of the received wavefront (right). In both cases, the distribution of the optimal pointing azimuths is uniform in the  $[0, 2\pi]$  interval. The origin is the direction of the  $z$  axis.

The observations of fractional powers slightly exceeding one are due to fortuitous corrections of the off-axis propagation originated by the coma.

Figure 9 shows the quadratic average over  $10^4$  Monte Carlo calculations of the root mean square amplitude  $\sigma_w$  of the phase noise when the jitters of the horizontal and vertical tilts ( $\alpha_x$  and  $\alpha_y$ ) are uncorrelated white noises having 10 nrad standard deviations. The average is given both versus the pointing deviation from the  $z$  axis and the output-plane coordinates. Figure 10 shows the  $\sigma_w$  distribution when the beam is transmitted along the  $z$  axis. When the transmitting telescope points in a cone having 100 nrad half-aperture about the  $z$  axis, the

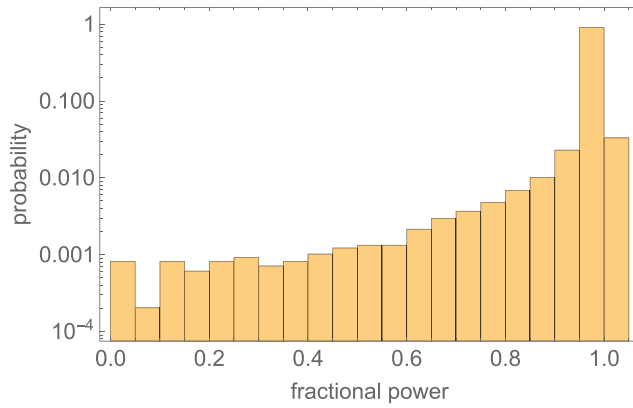


**Figure 8.** Histogram of  $10^4$  Monte Carlo calculations of the received (fractional) power. The laser beam is transmitted in such a way to minimise the phase noise of the received wavefront.

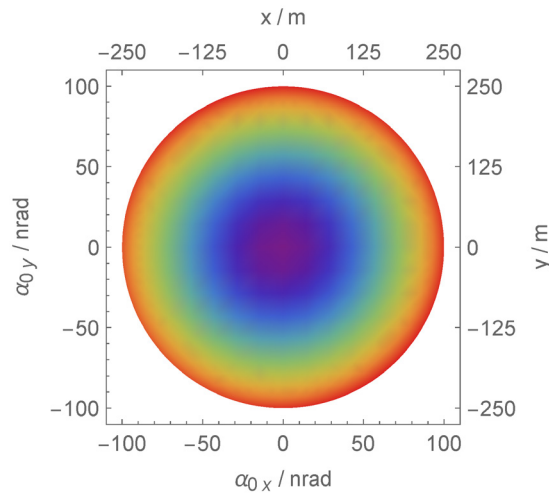


**Figure 9.** Mean phase-noise (quadratic average of the root mean square amplitudes) of the received wavefront.  $\alpha_{0x}$  and  $\alpha_{0y}$  are the mean horizontal and vertical tilts of the transmitted wavefront, where the origin identifies the  $z$  axis.  $x = \alpha_{0x}z$  and  $y = \alpha_{0y}z$  are the transverse coordinates at the receiving telescope. The rainbow ranges from 0.8 pm to 1.0 pm. The (horizontal and vertical) tilt jitters of the transmitted wavefront (10 nrad standard deviation) are white and uncorrelated. The errors of the transmitted wavefront are constrained to  $\lambda/20$ . The means are calculated over  $10^4$  Monte Carlo simulations.

expected  $\sigma_w$  value is about 0.9 pm. The distribution of the tilt magnitude is a Rayleigh one having  $\sqrt{\pi/2} \sigma_{x,y}$  mean. Therefore, 0.9 pm standard deviation (mean value) of the phase noise corresponds to a  $w(0; z)$  sensitivity to the tilt equal to  $\pm 0.07 \text{ pm nrad}^{-1}$ , which is in excellent agreement with the previous estimate based on the figure 5 data. To establish criteria for quality of the transmitted wavefront, we repeated Monte Carlo calculations in the case of arbitrary  $\lambda/10$  and  $\lambda/40$  aberrations. Table 3 shows the results.

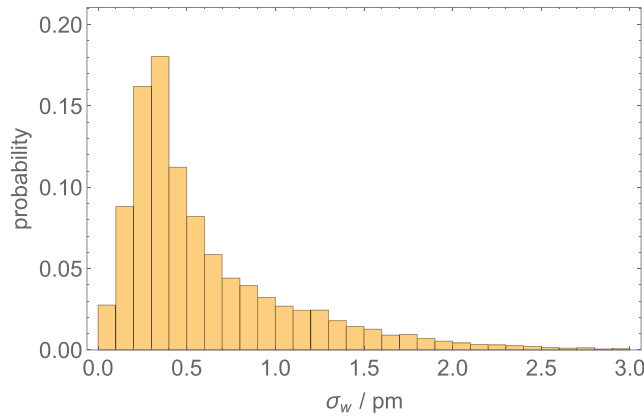


**Figure 10.** Histogram of  $10^4$  Monte Carlo calculations of the phase noise  $\sigma_w$  (root mean square amplitude) originated by the coupling of the (horizontal and vertical) tilt jitter (10 nrad standard deviation, white, and uncorrelated) with random  $\lambda/20$  errors of the transmitted wavefront. The beam is transmitted along the  $z$  axis.

**Table 3.** Sensitivity (expressed in  $\text{pm nrad}^{-1}$ ) of the received-wavefront phase to the tilt of the transmitted wavefront for (arbitrary) aberrations of the same constrained to  $\lambda/10$ ,  $\lambda/20$ , and  $\lambda/40$  deviations from a flat. The beam is transmitted along the  $z$  axis.

$\lambda/10$	$\lambda/20$	$\lambda/40$
$\pm 0.28$	$\pm 0.07$	$\pm 0.02$

## 7. Conclusions

A gravitational wave shifts the phase of the laser beams linking the LISA’s spacecraft by less than 10 pm. To compensate for the disturbances, the beam pointing is continuously corrected, which corrections jitter the transmitted wavefront [20]. If the received wavefront is spherical and centred on the test mass, the pointing jitter does not affect its phase. However, if the outgoing wavefront is aberrated, the phase of the received wavefront varies, and the jitter-induced noise must be made harmless.

We carried out analytical computations to determine the wavefront error at the receiving spacecraft as a function of lowest-order Zernike aberrations of the transmitted wavefront. Calculations were done both for flat and Gaussian intensity profiles, the former having been used to validate the Gaussian results via a cross check in the appropriate limit case. Next, we obtained an analytical expression of the phase noise and used it to carry out Monte Carlo calculations in the case of arbitrary aberrations of the transmitted wavefront—constrained to a given optical flatness—and horizontal and vertical jitters having 10 nrad root mean square amplitudes.

The sensitivity to the jitter is minimised when the laser beam points in a direction that, in general, deviates from that of the receiving spacecraft. Almost always this implies a negligible loss of the transmitted power, but there exist cases where the power loss is higher

than 50%. Without optimisation, the sensitivity to the jitter increases (non-linearly) from  $\pm 0.02 \text{ pm nrad}^{-1}$  to  $\pm 0.28 \text{ pm nrad}^{-1}$  when the optical quality of the transmitted wavefront decreases from  $\lambda/40$  to  $\lambda/10$ .

We assumed that aberrations other than defocus, astigmatism coma, trefoil and spherical are negligibly smaller. This assumption might be too optimistic. In fact, in a combined x-ray and optical interferometer used to determine the lattice parameter of silicon, the comparison of the wavefront of the optical beam—having about 3 mm  $1/e^2$  diameter—to the crystal lattice planes highlighted errors as large as  $\lambda/10$  having a periodicity of less than 1 mm [21, 22]. They were most probably due to imperfections of the surfaces hit or crossed by the laser beam. This observation suggests that the Zernike spectrum of the transmitted wavefront might have high-frequency components originated in the beam path through the optical bench and transmitting telescope. Therefore, future work must examine the impact of high-frequency aberrations on the far field propagation.

## Acknowledgments

This work was funded by the European Space Agency (contract 1550005721, Metrology Telescope Design for a Gravitational Wave Observatory Mission).

## ORCID iDs

C P Sasso  <https://orcid.org/0000-0002-5715-7688>

G Mana  <https://orcid.org/0000-0002-4109-7254>

## References

- [1] ESA 2007 Lisa phase 0 CDF study—internal final presentation <http://sci.esa.int/lisa/59336-lisa-internal-phase-0-cdf-study-final-presentation/> (accessed: 10 April 2018)
- [2] ESA 2016 The ESA L3 gravitational wave mission final report <https://cosmos.esa.int/documents/427239/653121/goat-final-rev1.pdf/> (accessed: 10 April 2018)
- [3] Danzmann K 2017 LISA Laser Interferometer Space Antenna—a proposal in response to the ESA call for L3 mission concepts [www.elisascience.org/files/publications/LISA\\_L3\\_20170120.pdf](http://www.elisascience.org/files/publications/LISA_L3_20170120.pdf) (accessed: 10 April 2018)
- [4] Livas J C, Arsenovic P, Crow J A, Hill P C, Howard J M, Seals L T and Shiri S 2013 *Opt. Eng.* **52** 52
- [5] Livas J, Sankar S, West G, Seals L, Howard J and Fitzsimons E 2017 *J. Phys.: Conf. Ser.* **840** 012015
- [6] Jennrich O 2009 *Class. Quantum Grav.* **26** 153001
- [7] Robertson D and Hough J 1996 *Class. Quantum Grav.* **13** A271
- [8] Thorpe J I 2010 *Class. Quantum Grav.* **27** 084008
- [9] Weise D, Braxmaier C, Gath P, Schulte H R and Johann U 2017 Optical metrology subsystem of the LISA gravitational wave detector *Proc. SPIE* **10567** 10567
- [10] Robertson D I, McNamara P, Ward H and Hough J 1997 *Class. Quantum Grav.* **14** 1575
- [11] Vinet J Y personal communication (2017)
- [12] Caldwell M, McNamara P and Glennmar A 1998 Optical engineering requirements for the LISA wavefront error budget *Laser Interferometer Space Antenna, Second Int. LISA Symp. on the Detection and Observation of Gravitational Waves in Space (American Institute of Physics Conf. Series vol 456)* ed W M Folkner (Woodbury, New York: American Institute of Physics) pp 156–64
- [13] Waluschka E 1999 Lisa far-field phase patterns *Proc. SPIE* **3779** 3779
- [14] Papalexandris M V and Waluschka E 2003 *Opt. Eng.* **42** 1029–37

- [15] Winkler W 1997 *Class. Quantum Grav.* **14** 1579
- [16] Bender P L 2005 *Class. Quantum Grav.* **22** S339
- [17] Sanjuan J, Korytov D, Mueller G, Spannagel R, Braxmaier C, Preston A and Livas J 2012 *Rev. Sci. Instrum.* **83** 116107
- [18] Goodman J 1996 *Introduction to Fourier Optics (Electrical Engineering Series)* (New York: McGraw-Hill)
- [19] Wolfram Research, Inc. 2017 *Mathematica, Version 11.2* (Champaign, IL: Wolfram Research, Inc.)
- [20] Dong Y H, Liu H S, Luo Z R, Li Y Q and Jin G 2014 *Rev. Sci. Instrum.* **85** 074501
- [21] Balsamo A, Cavagnero G, Mana G and Massa E 2003 *J. Opt. A: Pure Appl. Opt.* **5** 418
- [22] Sasso C P, Massa E and Mana G 2016 *Opt. Express* **24** 6522–31